Decoding Excimer Formation in Covalent Organic Frameworks Induced by Morphology and Ring Torsion

Jeet Chakraborty[a], Amrita Chatterjee[a], Korneel Molkens[b,c,g], Ipsita Nath[a], Daniel Arenas Esteban[d], Laurens Bourda[a,e], Geert Watson[a], Chunhui Liu[a,f], Dries van Thourhout[c,g], Sara Bals[d], Pieter Geiregat[b,c]*, Pascal Van der Voort[a]*

[a]   Centre for Ordered Materials, Organometallics and Catalysis (COMOC), Department of Chemistry, Ghent University, Krijgslaan 281-S3, 9000 Ghent, Belgium.

[b]   Physics and Chemistry of Nanostructures, Department of Chemistry, Ghent University, Krijgslaan 281-S3, 9000 Ghent, Belgium.

[c]   NOLIMITS, Center for Non-Linear Microscopy and Spectroscopy, Ghent University, Krijgslaan 281-S3, 9000 Ghent, Belgium.

[d]   EMAT-Electron Microscopy for Materials Science, Department of Physics, University of Antwerp, Groenenborgerlaan 171, 2020, Antwerp, Belgium.

[e]   XStruct, Department of Chemistry, Ghent University, Krijgslaan 281-S3, 9000 Ghent, Belgium.

[f]   NanoSensing Group, Department of Chemistry, Ghent University, Krijgslaan 281S3, 9000 Ghent, Belgium.

[g]   Photonics research group, Department of Information Technology, Ghent university – imec, Technologiepark-Zwijnaarde 126, 9052 Ghent, Belgium.

Corresponding authors: Pieter.Geiregat@Ugent.be; Pascal.VanDerVoort@Ugent.be

Abstract

A thorough and quantitative understanding of the fate of excitons in Covalent Organic Frameworks (COFs) after photoexcitation is essential for their augmented optoelectronic and photocatalytic applications *via* precise structure tuning. We herein report the synthesis of a library of COFs having identical chemical backbone with impeded conjugation, but varied morphology and surface topography to study the effect of these physical properties on the

photophysics of the materials. The variation of crystallite size and surface topography substantified different aggregation pattern in the COFs, which led to disparities in their photoexcitation and relaxation properties. Depending on aggregation, an inverse correlation between bulk luminescence decay time and exciton binding energy of the materials was perceived. Further transient absorption spectroscopic analysis confirmed the presence of highly localized, immobile, Frenkel excitons (of diameter 0.3-0.5 nm) *via* an absence of annihilation at high density, most likely induced by structural torsion of the COF skeletons, which in turn preferentially relaxes *via* long-lived (nanosecond to microsecond) excimer formation (in femtosecond scale) over direct emission. These insights underpin the importance of structural and topological design of COFs for their targeted use in photocatalysis.

Introduction

Covalent Organic Frameworks (COFs) are a surging class of lightweight ordered extended organic networks.[1-4] The permanent nano-porosity and high surface area of COFs make them efficient heterogeneous catalysts/scaffolds.[5,6] A manual control over the choice of organic monomers featuring distinct properties further aids the targeted use of COFs. In particular, the ability to choose monomers with appropriate redox and electron donor-acceptor properties from the wide arsenal of organic building blocks endows us with a switch to tune the overall redox properties and localized polarizability in the resultant COF networks.[7-9] Moreover, the robust covalent bonds in COFs are not prone to reduction and oxidation under typical light-initiated processes. Additionally, extended two-dimensional (2D) COF sheets often manifest a lamellar stacking, further easing the excited-state charge transport in the material across all dimensions and lending them semiconducting properties.[10-13] A combination of these features led to the extensive use of these materials in photocatalysis and optoelectronics.[14-17]

Despite ample adaptation of 2D COFs as efficient photo-responsive materials, their consorted photophysical and physicochemical scene at molecular level across widely different time (from fs to ms) and length scales (nm), *e.g.*, the initial photo-excitation event, exciton size lifetime and delocalization, charge separation and dynamics within the framework and at the framework-medium (*i.e.*, solvent or gas molecules) interface, etc. is still very much a black box. Regardless of a global intuitive idea of tailoring COFs' properties by tuning their monomers and/or synthetic conditions,[18,19] little is known about the fundamental

[2]

niceties of structure-property-guided charge dynamics in these materials. Bien, Rao, Friend and co-workers showed that in fully conjugated 2D COFs featuring distinct electron-donor and acceptor sites, photo-induction can generate bound singlet excitons that can travel through the COF plane, eventually leading to an exciton-exciton annihilation (EEA) followed by trap-like charge separation.[20] Varying the pump-fluence in transient absorption (TA) spectroscopy was used as a tool to stimulate the EEA process, which proceeds on sub-100 ps timescales. Jiang and Scholes *et al* also came to a similar understanding for their bulk-phase 2D COFs.[21] Recently, Chen, Dichtel and co-workers also adopted a similar pump power dependent strategy to study the excitation profile and charge dynamics in 2D COF-5 colloidal nanosheets of *ca.* 20-40 nm domain size.[22-24] The transient absorption kinetic trace analysis allowed them to underpin the generation of excimers upon relaxation of the excitons across adjacent sheets, providing further insights into the excited state dynamics.

Such excimers are typically long-lived species with a charge-separated nature.[25] Therefore, if formed on COF surface that is easily reachable by other molecules, they can be potentially beneficial in photocatalysis. From this perspective, an EEA, encountered routinely due to extended exciton mobility, can even be detrimental for photocatalysis where direct charge transfer takes place between the catalyst and the reaction mixture. However, little has been known to induce preferential excimer formation in COFs for their augmented use in photocatalysis.[26,27] Additionally, though the aforementioned seminal contributions paved the fundamental understanding of excited state charge dynamics in proto-typical COFs, the translation of these observations to the bulk materials that are routinely employed in photocatalysis remained underexplored as well. Understanding the correlation between structural conjugation, morphology, and surface topography of bulk COFs to the exciton diffusion, EEA and/or excimer formation followed by their interfacial charge transfer ability to the adjacent medium/environment is pivotal for the design of these materials and to appreciate the most of their photocatalytic efficiencies. Driven by this idea, we herein report the synthesis of a library of imine-linked COFs with a constrained conjugation featuring identical chemical backbone but varied surface topography. The excited-state charge dynamics in these materials have been studied, followed by their charge transfer efficiency to the environment. The timescales for the entire charge dynamic process have been explored and a correlation has been made to propose a general scene of the photoexcitation-catalysis merger in COFs.

Result and Discussion

Schiff base condensation between 4,4',4"-(1,3,5-triazine-2,4,6-triyl)trianiline and 5,5',5"-(benzene-1,3,5-triyl)tripicolinaldehyde (TTA and BTPA, respectively) under solvothermal condition was used to obtain the targeted COF, TTA-BTPA (Fig. 1a). A series of this COF was prepared by varying the synthesis time while maintaining all other aspects identical (for details, *cf.* Supporting Information). Accordingly, nine versions of the COF were obtained and are denoted as TTA-BTPA-X, where X represents the synthesis time, *i.e.*, 0.5h, 2h, 4h, 6h, 8h, 9h, 12h, 24h, and 72h. The synthesis of the TTA-BTPA-Xs were confirmed by powder X-ray diffraction (XRD), X-ray photoelectron spectroscopy (XPS), Solid-state ^{13}C NMR, and Fourier transformed infrared (FTIR) spectroscopy. FTIR analysis showed that the peaks arising from the aldehyde C=O stretching of BTPA at *ca.* 1700 cm^{-1} and the amine N─H stretching of TTA at *ca.* 3400 cm^{-1} disappeared in all COFs, whereas a new peak appeared at *ca.* 1620 cm^{-1} that can be ascribed to the newly formed imine linkage (Fig. S1 and S2). XPS analysis further confirmed the synthesis of TTA-BTPA (Fig. S3). The deconvoluted high resolution C1s XPS showed two peaks centered at 284.07 and 285.18 eV, which can be ascribed to the graphitic C and C=N species in the COF respectively. Accordingly, N1s XPS also showed two peaks at 398.16 and 399.24 eV originating from the C=N units in pyridine and triazine, and the imine N respectively. On the other hand, solid-state ^{13}C NMR showed two significant peaks at 170 and 151 ppm arising from the carbons in triazine and imine, respectively (Fig. S4). Additionally, the deconvoluted NMR spectra showed peaks for other aromatic carbons in 120-140 ppm range.

The XRD patterns of all COFs showed excellent crystallinity. A strong peak at 4.0° can be seen in the XRD originating from the diffraction by (100) crystal plane. Additionally, signals for the diffraction from (110), (200), (210) and (220) crystal planes appeared at 7.1°, 8.2°, 10.8°, and 14.7°, respectively. The experimental XRD patterns matched well with the density functional theory (DFT) optimized simulated AA-stacked model of the material (Fig. 1b, 1c, S5), endorsing the stacked layer structure of the materials. On the other hand, the simulated AB-stacked model showed no resemblance to the experimental XRD patterns (Fig. S6). Even though strong crystalline reflections are obtained, a broad band at 25.3° could also be observed, indicating the presence of some amorphous material.
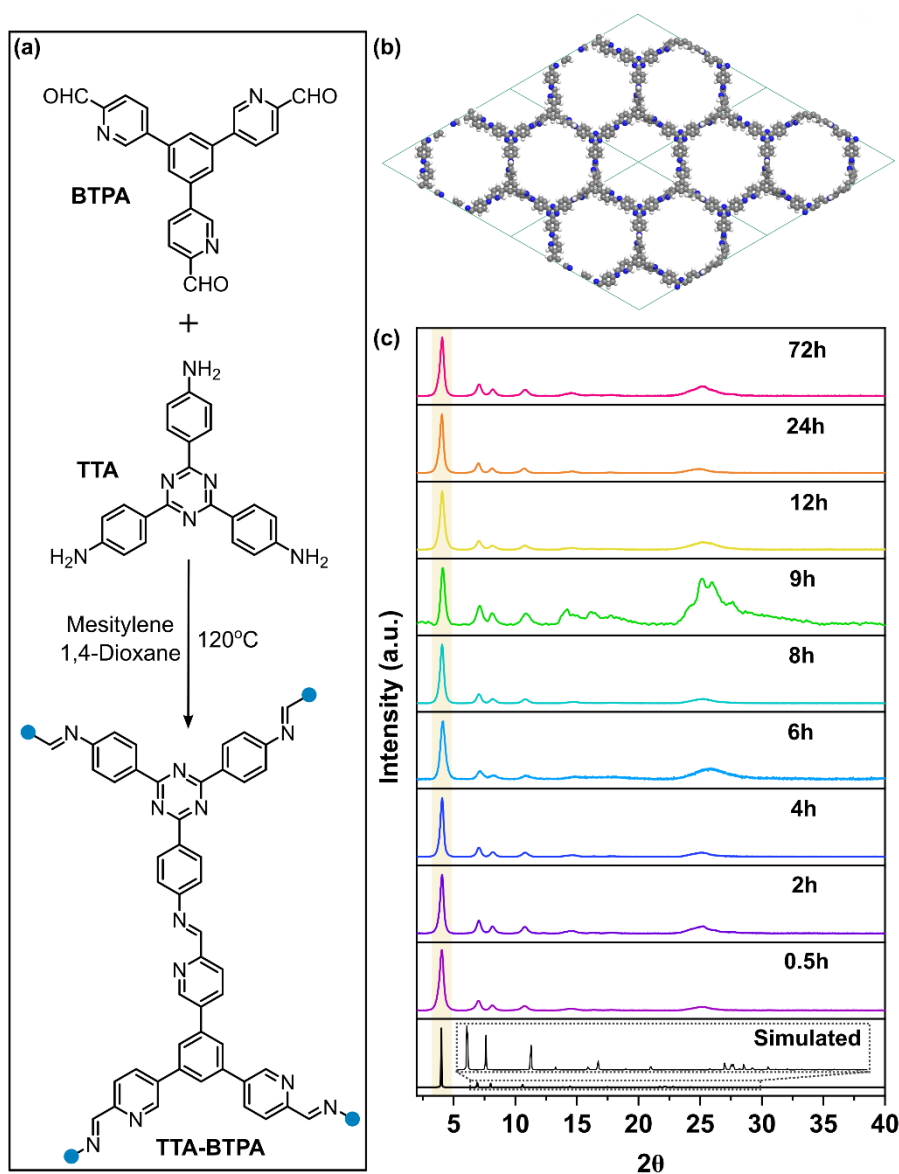
Figure 1. (a) Synthetic scheme of TTA-BTPA-X from the monomers, TTA and BTPA; (b) DFT optimized structure of TTA-BTPA-X; and (c) XRD patterns of the COFs compared to the simulated diffractogram obtained from DFT optmized AA-stacked model.

Nonetheless, all COFs showed analogous XRD patterns, owing to their identical chemical backbone and network formation, the extent of crystallinity of the materials differed with the synthesis time (in the range of *ca.* 65% to 85%). However, this change in crystallinity did not follow a linear correlation with the synthesis time (Fig. S7). A similar observation was perceived for the crystallite domain size as well. The full width half maxima (FWHM) of the TTA-BTPA-X diffractograms, used here as a measure of crystallite size following the Scherrer relation, showed no apparent correlation with the crystallinity of the samples (Fig. S7). We speculated that the highly polycrystalline nature of COF particles may justify this

[5]

apparent randomized trend despite the high crystallinity. Accordingly, electron microscopic techniques were opted to assess the surface topography and morphological evolution of the COF crystals. Transmission electron microscopy (TEM) investigations of TTA-BTPA-X captured the gradual growth of the COF crystals over time (Fig. S8). At 0.5 h, small COF particles (TTA-BTPA-0.5) of *ca.* 150 nm×50 nm dimensions started to emerge that formed agglomerations of random sizes (*ca.* 500 nm). The size of the agglomerates grew over time forming micrometer sized particles in 2 h. The laminar porous structure of TTA-BTPA-2 could be perceived by high-angle annular dark-field scanning transmission electron microscopy (HAADF-STEM), from which a pore diameter of *ca.* 1.9 nm was measured (Fig. S9), close to 2.1 nm diameter of the theoretically computed TTA-BTPA (Fig. 1b). This minor discrepancy can be justified by the effect of the electron beam during imaging, which often results in sample shrinkage in HAADF STEM.[28] The 3D tomography of the COF did not indicate a significant surface topography (Fig. 2b). However, upon further increasing the synthesis time, needle type growth of the COF particles on the bulk surface started to become evident. These needles became more well-defined for TTA-BTPA-6, while simultaneous agglomeration of the COF particles continued. TEM analysis indicated that this trend continued on increasing the synthesis time (Fig.2a). The surface electron tomography of TTA-BTPA-X shed further light on the growth pattern of the COF needles (Fig. 2b, Supporting video 1). After reaching a distinctive population (in TTA-BTPA-8), the needles manifested more in-plane growth, *i.e.*, increased more on width than length over time (in TTA-BTPA-24, Fig. 2). On further increase in reaction time, they resumed to grow longitudinally as well (in TTA-BTPA-72, Fig. 2). Of note, the laminar structure and crystal fringes of the COFs can be seen from HAADF-STEM, further confirming their highly crystalline nature. The diameters of the COF pores were measured to be 2.1 nm, which is identical to the DFT optimized model. This dynamic growth of the COF needles, together with simultaneous bulk particle agglomeration can be correlated to the non-uniform change in crystallinity and crystallite size as perceived from the XRD. The topological evolution of the COF was additionally studied by scanning electron microscopy (SEM) as well. SEM images also endorsed an identical time-dependent COF growth patten as perceived by TEM (Fig. S10).
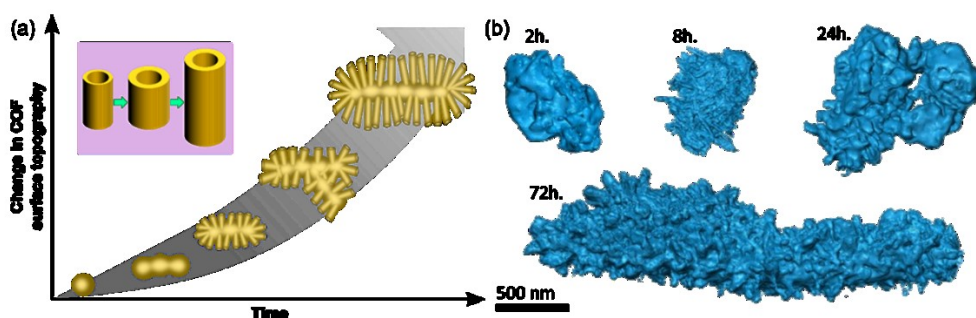
Figure 2. (a) Schematic model of the changes in COF surface topography perceived over time. (b) Images of the 3D reconstructed volumes for TTA-BTPA-X synthesized at 2, 8, 24, and 72 hours.

The DFT optimized model COF showed that due to steric repulsion between the *ortho* hydrogens of the central phenyl ring and the pyridine rings in BTPA, a torsional angle of *ca.* 53° exists between these rings (Fig. 3).[29,30] Accordingly, two of the three imine linkages formed by BTPA in the COF also manifested 53° angle with the 2D COF plane, whereas the third one maintained a 19° angle. This torsional degree suggested an improper orbital overlap leading to impeded extended electronic conjugation. The total electron density mapping of the theoretical model indeed showed discontinued conjugation at the rotated imine sites (Fig. 3). The distance between the planer aromatic systems adjacent to this imine was calculated to be 1.04 nm. On the other hand, the distance between the COF 2D sheets were obtained as 3.51 nm. These distances suggested that despite impeded conjugation, a Förster-type excitonic energy transfer can occur spatially both within and across the COF planes.[31] By translating this scenario to the topographic evolution of COF particles, it can be speculated that the in-plane and longitudinal development dynamics of TTA-BTPA-X needles would significantly affect the charge transport in the materials. Accordingly, the photophysical and optoelectronic properties of TTA-BTPA-Xs were studied to comprehend this hypothesis.
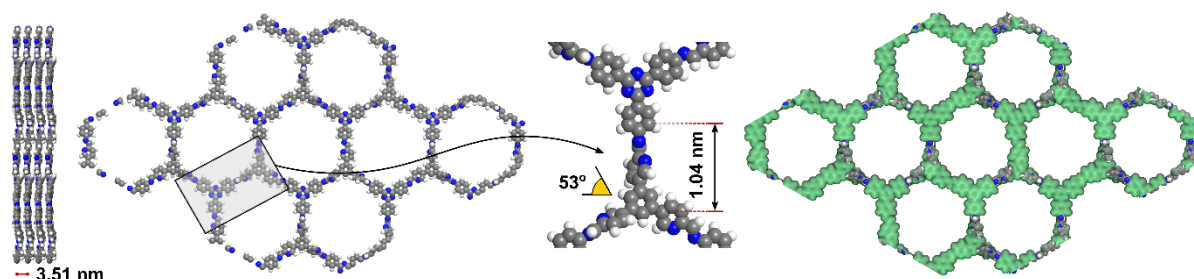
Figure 3. DFT optimized model of TTA-BTA showing a stacking distance of 3.51 nm between the COF layers, torsion of the chemical backbone, and impeded electronic delocalization resulted due to this torsion.

[7]

Photo-absorption maxima for all COFs was located at 420 nm in the normalized solid-state UV-Vis absorption spectra (Fig. 4a). Additionally, with increasing COF synthesis time, a broadening of the absorption edge at *ca.* 500-700 nm was be observed, indicating an enhanced charge separation in the material. Optical bandgaps (E_{OPT}) of the materials calculated from the corresponding Kubelka-Munk plots (Fig. 4a inset, S11) varied in an extended range of 2.65 to 2.79 eV depending on the synthesis time, *ergo* surface topography (Table 1). To date, a myriad of literature reported the alteration of COF bandgaps by changing the constituent monomers, owing to their distinct redox potentials.[16,17] However, a topography-induced change in bandgap of bulk COFs, featuring identical chemical backbone, have rarely been reported. Judging by the intra- and inter-layer distance between the planer units of TTA-BTPA-X (serving as chromophores) and the needle-type growth pattern of the materials, we hypothesized that the bulk COF structures could be rationalized as organic chromophore aggregates.[20] As such, the highly crystalline orientation of these units in the 2D COF planes and across z-direction (*i.e.*, gradual growth of the COF needles along width and hight as a function of time, as endorsed by electron microscopic analysis) can be translated into head-to-tail J-type and head-to-head H-type aggregates, respectively.[12] Considering the time-dependent topographic dynamics, the bulk COFs would, therefore, exhibit H-J coupling (Fig. 4c).
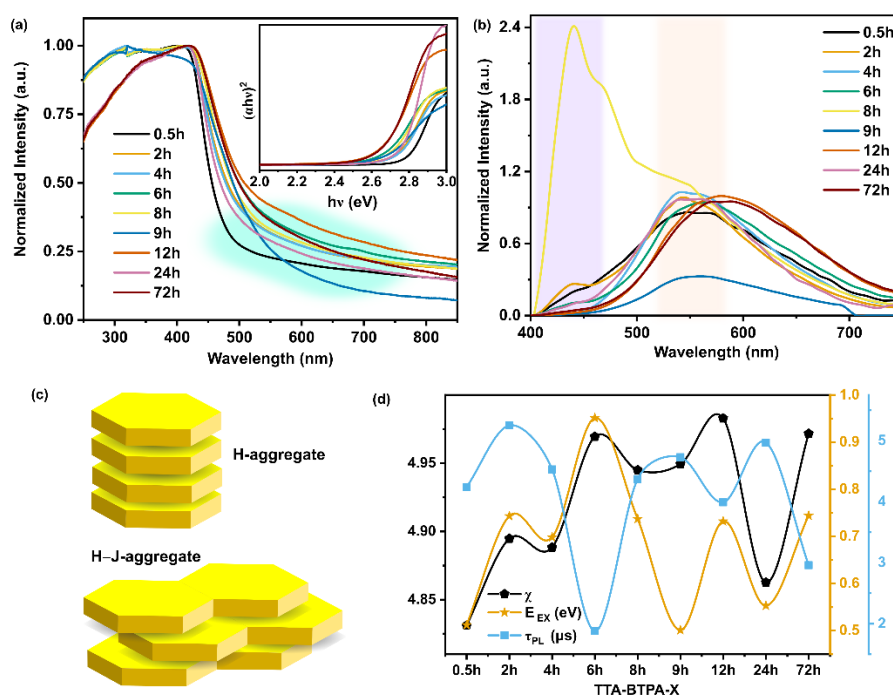
Figure 4. (a) Solid-state diffuse reflectance UV-Vis spectra of TTA-BTPA-X; (b) Photoluminiscence spectra of the COFs showing H-aggregation (purple shade) and J

[8]

To substantiate this aggregation theory, photoluminescence (PL) spectra of the COFs were recorded (Fig. 4b). All versions of TTA-BTPA-X showed a low-energy peak at *ca.* 550 nm in the PL normalized against respective absorption maximum from the excitation spectra (at λ_{EX} = 370 nm). A second distinct high-energy feature at *ca.* 440 nm was observed in the COFs synthesized under short reaction period (*i.e.,* at X = 0.5 to 8). Considering the longitudinal growth of the TTA-BTPA-X needles at the early stage of synthesis as observed by electron tomography, they were expected to manifest a preferential H-aggregate nature. This led to enhanced vibronic coupling of the 0-0 and 0-1 Franck Condon states resulting in blue emission.[32,33] As proposed by Spano and colleagues, the coherence length (N_{Coh}) of the aggregates can be calculated from the relative ratio of the 0-0 and 0-1 peak intensity (I^{0-0} and I^{0-1}) as a direct measure to estimate their vibronic couplings using the formula:[34]

$$N_{Coh} = k^2 \frac{I^{0-0}}{I^{0-1}}$$

Eqn. 1

where *k* is Huang−Rhys factor that depends on the monomers. By fitting the PL spectra of TTA-BTPA-Xs exhibiting H-type aggregation to normal distribution, I^{0-0} and I^{0-1} can be obtained (Fig. S12, S13), whereas the *k*-factor would remain identical for all COFs.[33] Accordingly, the ratio of the coherence length for TTA-BTPA-2 and TTA-BTPA-8 was calculated as 1.5, suggesting that at an early stage of the synthesis, the COF would manifest a preferential H-aggregation which would gradually shift to a H-J aggregation over extended synthesis period. The low-energy PL component (at 550 nm, Fig. 4b) arising from the H-J coupling was present in all COFs. Compared to TTA-BTPA-0.5, the normalized intensity of this green emitting peak slightly increased and remained almost constant for the other COFs (except the 9h version) suggesting that this feature is arising from the bulk agglomeration of the materials.

Notably, unlike the other versions of TTA-BTPA-X, the XRD of TTA-BTPA-9 (Fig. 1c, S5) showed a considerable decrease in the (100) peak intensity comparted to the diffractions from other planes. This observation indeed indicates a preferential orientation of the COF needles in this material such that the (100) crystal plane is limitedly exposed.[39] The SEM and TEM analysis provided further visual insights to this orientation (Fig. S14, S15). On the other hand,

[9]

contrary to the other materials, TTA-BTPA-9 exhibited significantly diminished normalized PL intensity despite having identical photo-absorption and excitation profile as the rest. By extrapolating the structural observations to the aggregation theory, we hypothesized that the change in COF needle orientations, *ergo* aggregation, preferentially induced a J-type feature to the overall H-J coupling. Such aggregation would result in the parallel orientation of the dipoles originated from the photo-induced charge separation in the material, justifying a decreased PL intensity.[36]

Table 1. Photophysical and optoelectronic parameters of TTA-BTPA-X.

TTA-BTPA-X	E_{OPT} (eV)	CBM (vs SCE)	VBM (vs SCE)	E_{FUND} (eV)	τ_{PL} (μs)	E_{EX} (eV)	n	ε_r	χ
0.5h	2.79	-0.58	2.73	3.31	4.24	0.51	2.41	5.83	4.83
2h	2.73	-0.69	2.79	3.48	5.25	0.74	2.43	5.89	4.89
4h	2.74	-0.71	2.73	3.44	4.53	0.70	2.43	5.89	4.89
6h	2.67	-0.83	2.79	3.62	1.88	0.95	2.44	5.97	4.97
8h	2.69	-0.74	2.69	3.43	4.37	0.74	2.44	5.94	4.94
9h	2.68	-0.73	2.46	3.19	4.73	0.50	2.44	5.95	4.95
12h	2.65	-0.61	2.78	3.39	3.99	0.73	2.45	5.98	4.98
24h	2.76	-0.53	2.79	3.32	4.97	0.55	2.42	5.86	4.86
72h	2.66	-0.68	2.73	3.41	2.96	0.74	2.44	5.97	4.97

Consequently, the decay profile of the low-energy PL peak measured for TTA-BTPA-X showed overall slow recombination of the charged pairs (Table 1). All the decay traces could be fitted to first-order exponential kinetics ($R^2 = 0.999$) with decay time (τ_{PL}) varying from 1.88 to 5.25 μs. To further understand the effect of aggregation on the photophysical and optoelectronic properties of the COFs, we calculated their electromagnetic susceptibility (χ) and exciton binding energy (E_{EX}) and plotted them against τ_{PL} (Fig. 4d). Differential pulse voltammogram was used to obtain the electronic valence band maxima (VBM) and

[10]

conduction band minima (CBM) of the COFs for calculating their fundamental bandgap (E_{FUND}, Fig. S16). E_{EX} was then calculated as the difference of E_{FUND} and E_{OPT}.[37] On the other hand, the empirical Moss equation (Eqn. 2) was used to calculate the refractive indices (*n*) of the COFs, which were then converted to respective χ following Eqn. 3.

$$n^4 \times E_{OPT} = 95 \ eV \qquad\qquad \text{Eqn. 2}$$

$$\chi = \varepsilon_r - 1 = n^2 - 1 \qquad\qquad \text{Eqn. 3}$$

where ε_r represents the relative permittivity of the materials (Table 1).

As shown in Fig. 4d, χ values for all COFs were found be proportional to respective E_{EX}. As χ can be visualized as a measure of the degree of photo-induced polarization of the COFs, its directly proportional nature with E_{EX} together with their dependence on the COF topography suggests that with increase in the H-aggregation, the polarization and exciton binding energy of TTA-BTPA-X increased. As the contribution of J coupling increases, E_{EX} and χ decreased again. The 6h to 12h COF synthesis window captures this dynamic well (Fig. 4d). Interestingly, TTA-BTPA-9 featuring maximum J-aggregate contribution exhibited the lowest E_{EX} but a relatively high χ. This indicates that the excited charges would be highly separated in this material, which can justify its extreme PL quenching. On the other hand, τ_{PL} mostly maintained an inverse proportionality with E_{EX}, which can be easily rationalized considering a higher Coulombic attraction (*i.e.*, E_{EX}) would lead to faster recombination of the charges, and *vice versa*.

As the microscopic, spectroscopic and photophysical analyses collectively indicated an overall volcano-type nuance of TTA-BTPA-X with an inflection at 8h to 9h synthesis window, we further analysed these two samples by ultrafast pump-probe TA spectroscopy. The band structure and partial density of states (PDOS) calculated for the theoretical model (bilayer) of the COF showed that the conduction band (CB) was comprised of *p*-orbitals, whereas both *s* and *p* orbitals contributed to the formation of the valence band (VB) (Fig. 5a). It can be justified considering that the non-conjugating lone *s*-electron pairs on the nitrogens of pyridine and triazine in the COF participates in the VB formation. Evidently, the band decomposed highest occupied molecular orbital (HOMO) and lowest unoccupied molecular orbital (LUMO) of the chromophores would possess similar gerade orbital symmetry, making the corresponding photo-excitation symmetry forbidden (Fig. S17, S18). As H-J aggregation of the bulk COFs instigates augmented spin-orbit coupling, the symmetry can become

sufficiently relaxed for the photoexcitation to become viable. The solution-state liner absorption profile of TTA-BTPA-8 and -9 indeed exhibited such partially symmetry allowed low-intensity peak with absorption maximum at 360 nm in NMP (Fig. 5b). Accordingly, the normalized TA spectral data of the two COFs (as dispersion in NMP) measured in the 370-900 nm wavelength window showed early ground state bleaching (GSB) at 370 nm. Additionally, three more typical features were observed in the TA spectra of both COFs, (i) a peak at *ca*. 400 nm ascribed to the excited state absorption (ESA), (ii) a fast depleting second peak at *ca.* 500 nm growing in the negative direction originating from stimulated emission (SE), and (iii) another low-energy near-IR photo-induced absorption (PIA) *ca.* 750 nm. A generic idealized scenario of the TA response is shown in the bottom panel of Fig. 5c together with the corresponding linear absorption (blue trace) and PL (brick red trace) on the top panel.
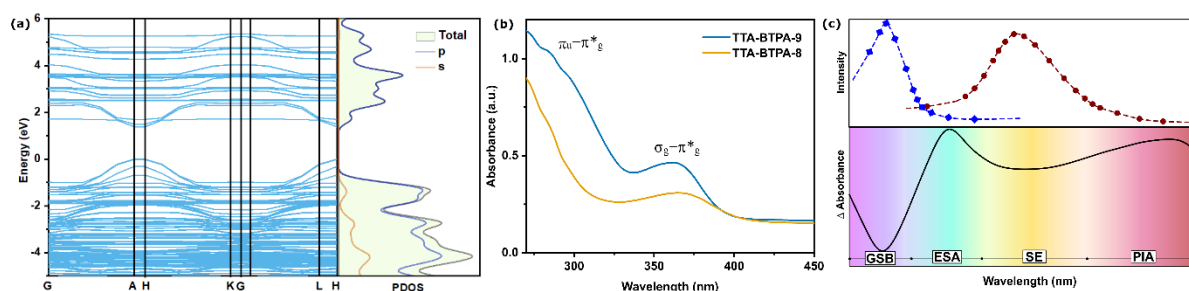
Figure 5. The band structure and partial density of states of TTA-BTPA (bilayer) calculated from the DFT optimized structure of the material; (b) Solution-state (in NMP) linear absorption spectra of TTA-BTPA-8 and -9; and (c) Schematic illustration of the different features of transient absorption spectra (bottom panel) and its inter-dependence with linear absorption (blue trace, top panel) and luminiscence (red trace, top panel).

As shown in Fig. 4b, the solid-state steady state PL emissions of TTA-BTPA-8 and -9 were centred at *ca.* 440 and 550 nm, respectively. This suggest a corresponding SE feature to be observed at 400-550 nm window in the TA spectra. Accordingly, in TTA-BTPA-8, an initial drop in absorbance was observed in 450-500 nm wavelength window at early probe delay till 10 ps (Fig. 6b). A similar observation was also recorded for TTA-BTPA-9, but in a slightly blue-shifted window of 420-500 nm (Fig. 7b). Of note, due to manual probe switching at 500 nm, we were unbale to record the complete SE response across the extended range (*i.e.* we could not measure at 480‒520 nm window). However, the tail of the SE can be seen in the 500 nm probe response of both COFs as well (Fig. 6e, 7e).

[12]
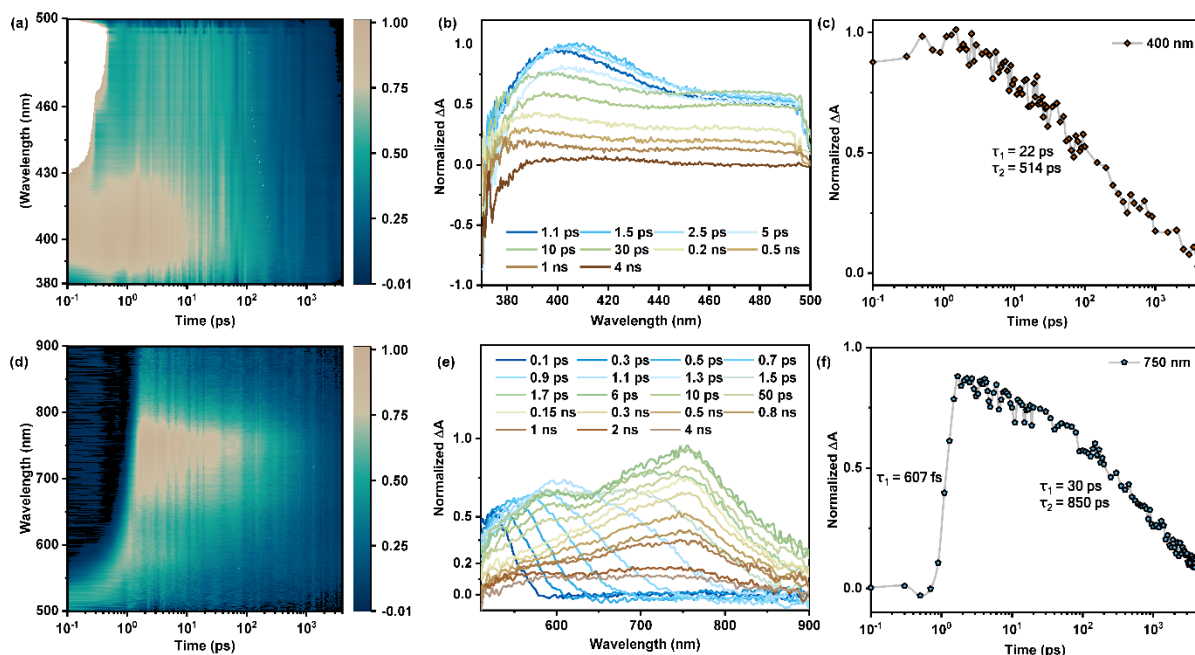
Figure 6. Contor plot of normalized TA spectra of TTA-BTPA-8 after photoexcitation with a 343 nm pump at 200 µJ/cm^2 fluence on a (a) 500 nm probe and (d) 900 nm probe with corresponding probe delay traces (b and e); kinetic traces of (c) 400 nm wavlength response and (f) 750 nm wavelength response.

Unlike other literature reports,[18-20] the intensity of the SE features of TTA-BTPA COFs were significantly low and masked by the adjacent high-energy ESA at 400 nm (Fig. 6b and 7b). This ESA represents a secondary photo-induced absorption of the excited singlet state, which can be comprehended as an $S_1 \rightarrow S_2$ transition from a molecular perspective. In case of TTA-BTPA, the ingrowth times for this ESA feature, a direct metric of the presence of excitons, were extremely fast (<270 fs). With increasing the pump fluence, *i.e.*, exposing the COF to higher amount of incident photons we can enhance the exciton formation, which would result in an increase in the ESA till a certain limit before the excitons starts to interact with each other leading to augmented exciton-exciton annihilation (EEA).[38] Thus, the EEA would result in a decrease in the ESA feature. We adopted this concept to understand the fate of excitons in our bulk COFs. Interestingly, no significant dependence of ESA on the pump fluence was observed (Fig. S19). Similarly, the SE and PIA did not show any dependence on pump fluence either (gradually increasing form 13 µJ/cm^2 to 200 µJ/cm^2). The decay of the ESA peaks for both COFs can be fitted to a bi-exponential function featuring two decay time constants, τ_1 and τ_2. Although the τ_2 values were similar for both COFs (530 ± 20 ps), the τ_1 for TTA-BTPA-9 (46 ps) was almost double of that of TTA-BTPA-8. This suggests that the decay of the ESA feature happens in two-steps, where both COFs goes through a common excited intermediate that decays at a slow rate (τ_2). The fast decay (τ_1) of the 8h sample

[13]

comparted to the 9h can be rationalized by their respective aggregation. Due to the Franck Condon overlap in the H-aggregated TTA-BTPA-8, the ESA relaxes faster. The slower τ_2 can then arguably be ascribed to the excitons in the H-J coupled aggregation of the materials (*i.e.* their bulk agglomerated phases).
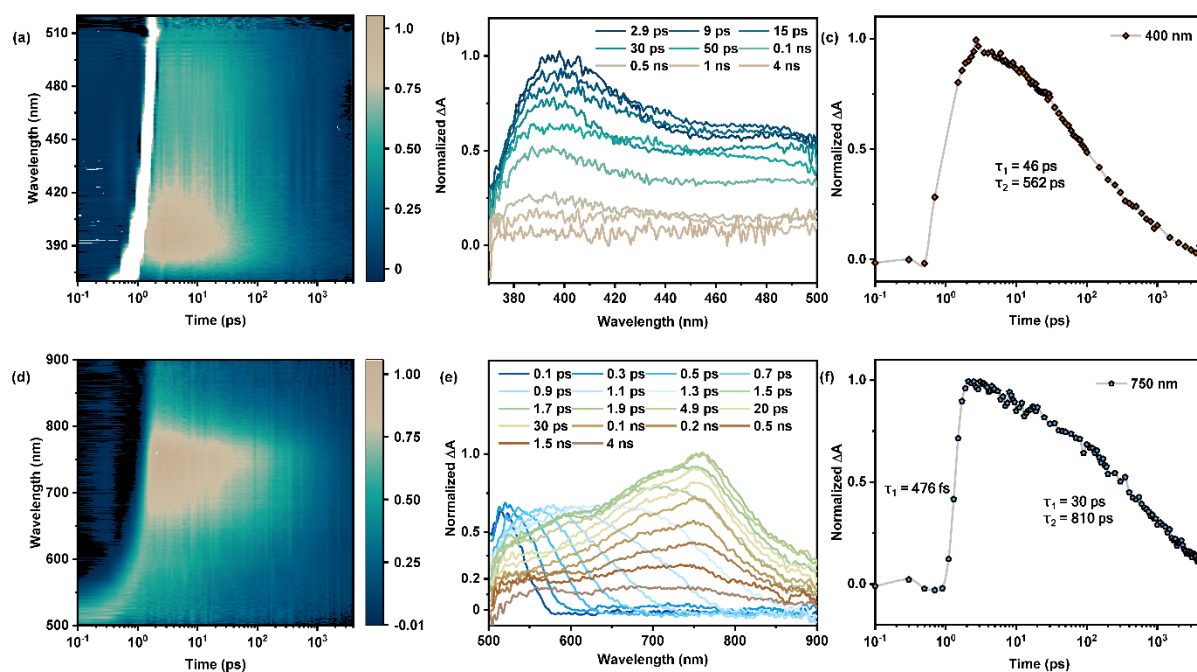
Figure 7. Contor plot of normalized TA spectra of TTA-BTPA-9 after photoexcitation with a 343 nm pump at 200 µJ/cm^2 fluence on a (a) 500 nm probe and (d) 900 nm probe with corresponding probe delay traces (b and e); kinetic traces of (c) 400 nm wavlength response and (f) 750 nm wavelength response.

In the shorter wavelength probe region shown in Fig. 7a and 7b, the SE of TTA-BTPA-9 appeared as a negative dip with λ_{MAX} at 480─500 nm. The SE of TTA-BTPA-8 also showed a similar pattern with a red-shifted λ_{MAX} (Fig. 6a, 6b). It has been previously corroborated by other groups that the SE feature can be tagged to the direct emission of the chromophores as well as to the spin-orbit coupling of the highly crystalline and ordered COFs.[19, 35] Considering the H and J type aggregation of the bulk COFs, we speculate that the exciton populations are depleting both in the co-facial manner as well as along the 2D planes *via* strong dipole-dipole coupling. Despite having identical chemical backbone, the difference in dipole-dipole coupling and orbital orientation at the local environment of the COF chromophores resulted in the energy shifts of their SE features.

The PIA feature at *ca*. 750 nm provided further insight into the excited state processes. For both COFs, the PIA decayed in a two-exponential pathway with similar time constants, τ_1 of

ca. 30 ps and τ_2 of *ca.* 830 ± 20 ps. On the other hand, both these PIA features grew in femtosecond timescale, where TTA-BTPA-9 possibly grew faster than -8 (Fig. 6f, 7f). This indicates that each material achieves the same excited species, which generates faster in the 9h sample but decays in a similar fashion. Given the slower growth rate of this PIA in comparison to the ESA at 400 nm, in addition to ~1 nm intra-facial and 3.5 nm co-facial distance between the dipole pairs (Fig. 3) in COFs, we speculate that this PIA feature is originating from the generation of excimer pairs.[40] Excimers can be visualized as a coupling between the excited state dipole (*i.e.* the exciton) and the ground state dipole, [21] which relaxes the original exciton to a certain extent *via* a Förster energy transfer pathway.

To this end, comparing the decay pattern of the PIA with that of the ESA, we considered the possibility of two competing excited state processes: (i) the excimeric relaxation of the excitons, which would require them to be highly localized, or (ii) rapid diffusion of the excitons across the COF due to enhanced tunnelling in the extended polycrystalline domain. Of note, the existence of both these process on organic semiconductors have previously been rationalized by other groups as well. However, as we could not see any EEA dependence of the pump fluence (even at a high fluence of 200 μJ/cm^2), a low mobility and a low occupancy of the exciton sites seems the only logical option. Indeed, if excitons cannot diffuse, by whichever mechanism, to encounter one another and if they do not pile up on sites themselves, no exciton-exciton annihilation should occur. We note that any linear trapping mechanisms would not be pump fluence activated. To numerically comprehend this hypothesis, we calculated the occupation probability (*f*) of an exciton site using Eqn. 4 and 5, where N_A is Avogadro number, ϵ is molar extinction coefficient obtained from linear absorption related to the individual sites of exciton absorption / creation (the chromophore unit of the COF structure), σ corresponds to absorption cross-section, and $N_{h\upsilon}$ represents photon density.

$$\sigma = \frac{\ln(10) \times \epsilon}{N_A} \qquad\qquad Eqn.\,4$$

$$f = N_{h\upsilon} \times \sigma \qquad\qquad Eqn.\,5$$

Accordingly, an *f* of 0.01 per chromophore was calculated at the highest pump fluence of 200 μJ/cm^2, which can be physically comprehended as the probability of generating an exciton in a chromophore unit constituting the COF is only one in a hundred. Translating this to the unit cell of the COF, we can realize that the probability of generating an exciton in one unit cell

would be 0.035 only. Now, looking back to the chemical structure of the COF, where each chromophore unit is electronically separated from the adjacent unit in plane by 1.04 nm *via* 53° torsional angle, and from the co-facial units by 3.51 nm, we can conject that extended delocalization of the excitons would be markedly impeded, as such they will be highly localized on individual chromophore. To further validate this, we calculated the Bohr diameter of the excitons (d_{EX}) by Eqn. 6, where a_0 is the Bohr radius of hydrogen.

$$d_{EX} = \frac{2 \times 13.6 \times a_0}{E_{EX} \times \varepsilon_r} \qquad Eqn.\,6$$

The d_{EX} for TTA-BTPA-8 was calculated to be 0.33 nm and that of TTA-BTPA-9 was 0.48 nm. On the other hand, the length of each planer chromophore units was calculated as 1.16 nm. These length scales together with strong E_{EX} can justify the Frenkel type nature of the excitons, and their partial mobility limited to individual chromophore sites. Combining this theory with the low f (0.035) per unit cell, we propose that when photo-irradiation generates an exciton in one chromophore, the adjacent chromophores remain in their ground state. The distance between these chromophores then allows a Förster energy transfer leading to the coupling of excitonic dipole and ground state dipole creating a relaxed excimer state (Fig. 8). Due to head-to-tail dipole orientation in the J-type TTA-BTPA-9, this coupling would be relatively faster. This can justify the faster ingrowth of the PIA feature in this sample compared to the 8h one. Additionally, this preferential excimer formation also explains the relatively low SE of the COFs compared to literature. Accordingly, photocurrent response of TTA-BTPA-8 and -9 were recorded in acetonitrile. As shown in Fig. S20, the 9h sample showed almost 1.5 times higher current density than the 8h counterpart when irradiated identically. Moreover, it also exhibited a slower decay rate of the current in dark. Considering a relatively lower E_{EX} and higher degree of aggregation-induced excimer formation in the 9h sample, its better photocurrent response is justified.

[16]
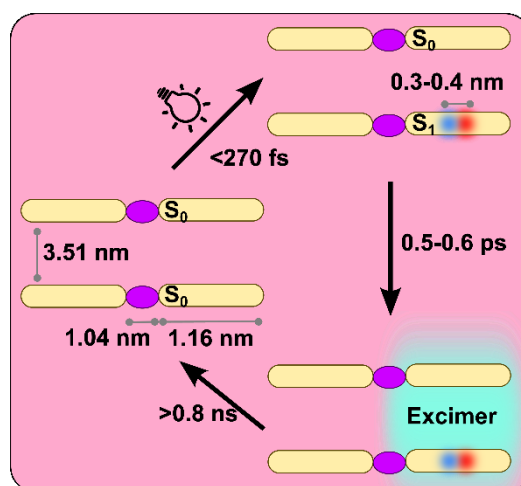
Figure 8. Schematic representation of the photoexcitation and relaxation of TTA-BTPA-X showing the time and length scale involved in the process, where the yellow bars represents a planer chromophore unit, the purple oval represents discontinuatiuon between the chromophores due to structural torsion, and the the blue and red shades stands for excited electron and hole.

To this end, as a tangible experimental validation to our claim, we subjected both TTA-BTPA-8 and -9 for photocatalytic hydrogen generation from water as a probe reaction using triethanolamine (TEOA) as a sacrificial hole scavenger without any co-catalyst. In line with the photophysical property trends, TTA-BTPA-9 indeed showed better photocatalytic performance than TTA-BTPA-8. Under identical condition, the 9h COF produced H_2 at a rate of 378 μmol/h/g_{cat}, about three times higher than the production rate of the 8h analogue, 132 μmol/h/g_{cat}. (Fig. S21). For better insight into the charge transfer process during the reductive H_2 evolution catalysis, we performed Mott-Schottky analysis of the COFs in water (pH = 7) in the reduction potential window of -0.1 V to -1.4 V(*vs* SCE) in the presence and absence of light (Fig. S22). Upon photo-illumination, the specific capacitance (C_s) increased for both COFs in the non-Faradaic-Faradaic inflection window, indicating the photo-triggered formation of augmented double layer. This observation is justifiable considering the induction of proton reduction in this potential window for the COFs. Interestingly, the C_s of TTA-BTPA-8 increased almost 1.4 times under light compared to only a nominal increase for TTA-BTPA-9. This observation can be tagged to the higher extent of excimer formation in the 9h-COF leading to a faster interfacial charge transport, which is also in line with the photocurrent response of the materials (Fig. S20).

As the role of surface topography and morphology of TTA-BTPA-Xs on their photo-response and catalytic performances were established, we further extended this theory to another COF system to assess the generality of our claims. Accordingly, another set of imine-linked COFs

was prepared by reacting BTPA and 1,3,5-*tris*-(4'-aminophenyl)benzene (TAPB) monomers for 12 and 72 h respectively. The produced COFs are denoted as TAPB-BTPA-X (where X = 12 and 72, Scheme S1). XRD analysis confirmed that both TAPB-BTPA-12 and -72 obtained as AA-stacked highly crystalline materials (Fig. S23). Similar to TTA-BTPA, the SEM and TEM images of these COFs also confirmed a time-dependent growth of the particles. TAPB-BTPA-12 appeared as an agglomeration of small flakes, whereas TAPB-BTPA-72 these flaks merged together to form hollow tubes (Fig. S24, S25). The optical bandgap of the materials calculated from the Tauc plot obtained from soldi-state UV-Vis spectra also showed that the 12h-COF featured a higher bandgap of 2.72 eV compared to 2.68 eV for the 72h analogue.

Since a similar trend of morphology-dependent change in optical bandgaps were observed in these COFs as that of TTA-BTPA-Xs, we further analysed the transient states of these COFs by fs-TA spectroscopy. As perceived from the SEM and TEM analysis, the longitudinal growth of TAPB-BTPA with time resulted in stronger ESA and PIA feature in the 72h-COF as compared to the 12h analogue (Fig. S27). Overall photo-response of the COFs also increased on increasing the synthesis time. The existence of PIA feature also indicated the existence of transient excimers in these COFs. Exponential fitting of the time component of normalized PIA feature showed that the ingrowth of excimer in TAPB-BTPA-72 is almost three times faster than that of TAPB-BTPA-12 (Fig. S28). However, it also decays faster in a bi-exponential manner. While the first time constant (τ_1) is similar for both materials, the second time constant (τ_2) is almost 1.5 times faster for the 72h analogue. These observations can be rationalized considering a higher degree of exciton formation in TAPB-BTPA-72 (*i.e.,* stronger ESA peak), which also enhances the corresponding excimer relaxation process, and thereby a faster ingrowth of the PIA. The long tubular shape of this COF can facilitate more H-type aggregation that can justify this phenomenon. However, it would also indicate a possibility of faster delocalization-induced decay, which may be tagged to the relatively fast decay of the PIA in the 72h material. On the other hand, the random agglomerated flakes of TAPA-BTPA-12 resulted in a more J-type aggregation pattern. A low exciton formation in this material may rationalize the relatively slower ingrowth of the PIA, whereas the preferential J-type aggregation led to slowed decay of the PIA, as also observed in TTA-BTPA system. Overall, these analyses confirmed that the morphology and topography of the COFs, which are induced by respective aggregation patterns, results in significant difference in the photophysical properties of the materials, despite their identical chemical backbone.

Conclusion

[18]

To propose a general photophysical scene for COF-based photocatalysts, we have found that the structural and morphological design of the material plays an equally important role as the chemical design. Despite identical chemical backbone, different topography of COFs can favour photoemission over catalysis and *vice versa*. A needle type growth of the COFs featuring planer structure would indicate a high degree of H-type aggregation in the material, that favours excitonic delocalization across the needle channel, making it a good photocurrent conductor. But it does not necessarily suggest an augmented photocatalytic performance as higher mobility of Frenkel type excitons would also result in a high degree of exciton annihilation, and thereby emission. However, it is interesting to note that as EEA would also generate a high energy triplet exciton, the needle shaped COFs can perform photosensitized reactions (*i.e.* the one that goes *via* energy transfer rather than a charge transfer) well.

Localization of the exciton in COFs *via* precise structural design, *e.g.*, by instigating restricted long-range conjugation, can enhance the highly desired long-lived excimer formation, which would favour a charge transfer to the medium, *ergo* photocatalysis. On the other hand, a poly crystalline feature often instigates a J-type aggregation in COFs, which in combination with localized excimers, further impedes emissive energy loss. Therefore, from this perspective, it can be concluded that polycrystalline COFs with limited electronic conjugation would be a great choice as a photocatalyst.

Acknowledgements

References

1) C. S. Diercks, O. M. Yaghi, *Science* 2017, **355**, eaal1585.

2) A. P. Cote, A. I. Benin, N. W. Ockwig, M. O'Keeffe, A. J. Matzger, O. M. Yaghi, *Science* 2005, **310**, 1166.

3) S. Kandambeth, K. Dey, R. Banerjee, *J. Am. Chem. Soc*. 2019, **141**, 1807.

4) F. Haase, B. V. Lotsch, *Chem. Soc. Rev.* 2020, **49**, 8469.

5) J. Guo, D. Jiang, *ACS Cent. Sci*. 2020, **6**, 869.

6) H.-Y. Cheng, T. Wang, *Adv. Synth.Catal.* 2021,**363**, 144.

7) Z. Chen, J. Wang, M. Hao, Y. Xie, X. Liu, H. Yang, G. I. N. Waterhouse, X. Wang, S. Ma, *Nat. Commun.* 2023, **14**, 1106.

8) N. Singh, D. Yadav, S. V. Mulay, J. Y. Kim, N.-J. Park, J.-O. Baeg, *ACS Appl. Mater. Interfaces* 2021, **13**, 14122.

9) X. Li, Q. Gao, J. Aneesh, H.-S. Xu, Z. Chen, W. Tang, C. Liu, X. Shi, K. V. Adarsh, Y. Lu, K. P. Loh, *Chem. Mater*. 2018, **30**, 5743.

10) C. R. Deblase, K. Hernández-Burgos, K. E. Silberstein, G. G. Rodríguez-Calero, R. P. Bisbey, H. D. Abruña, W. R. Dichtel, *ACS Nano* 2015, **9**, 3178.

11) J. Clark, C. Silva, R. H. Friend, F. C. Spano, *Rev. Lett.* 2007, **98**, 1.

12) H. Yamagata, F. C. Spano, *J. Chem. Phys.* 2012, **136**, 184901.

13) F. C. Spano, C.; Silva, *Annu. Rev. Phys. Chem*. 2014, **65**, 477.

14) H. Wang, H. Wang, Z. Wang, L. Tang, G. Zeng, P. Xu, M. Chen, T. Xiong, C. Zhou, X. Li, D. Huang, Y. Zhu, Z. Wang, J. Tang, *Chem. Soc. Rev*. 2020, **49**, 4135.

15) N. Keller, T. Bein, *Chem. Soc. Rev*. 2021, **50**, 1813.

16) L. Zhang, L. Yi, Z.-J. Sun, H. Deng, *Aggregate*, 2021, **2**, e24.

17) S. Yang, D. Streater, C. Fiankor, J. Zhang, J. Huang, *J. Am. Chem. Soc.* 2021, **143**, 1061.

18) Y. Xie, J. Li, C. Lin, B. Gui, C. Ji, D. Yuan, J. Sun, C. Wang, *J. Am. Chem. Soc*. 2021, **143**, 7279.

19) Y. Xia, W. Zhang, S. Yang, L. Wang, G. Yu, *Adv. Mater*. 2023, **35**, 2301190.

20) A. C. Jakowetz, T. F. Hinrichsen, L. Ascherl, T. Sick, M. Calik, F. Auras, D. D. Medina, R. H. Friend, A. Rao, T. Bein, *J. Am. Chem. Soc.* 2019, **141**, 11565.

21) X. Zhang, K. Geng, D. Jiang, G. D. Scholes, *J. Am. Chem. Soc.* 2022, **144**, 16423.

22) N. C. Flanders, M. S. Kirschner, P. Kim, T. J. Fauvell, A. M. Evans, W. Helweh, A. P. Spencer, R. D. Schaller, W. R. Dichtel, L. X. Chen, *J. Am. Chem. Soc*. 2020, **142**, 14957.

23) A. M. Evans, L. R. Parent, N. C. Flanders, R. P. Bisbey, E. Vitaku, M. S. Kirschner, R. D. Schaller, L. X. Chen, N. C. Gianneschi, W. R. Dichtel, *Science* 2018, **361**, 52.

24) B. J. Smith, L. R. Parent, A. C. Overholts, P. A. Beaucage, R. P. Bisbey, A. D. Chavez, N. Hwang, C. Park, A. M. Evans, N. C. Gianneschi, W. R. Dichtel, *ACS Cent. Sci*. 2017, **3**, 58.

25) J. B. Birks, *Nature* 1967, **214**, 1187.

26) O. P. Dimitriev, Y. P. Piryatinski, Y. L. Slominskii, *J. Phys. Chem. Lett*. 2018, **9**, 2138.

27) A. Das, A. Danao, S. Banerjee, A. Mohan Raj, G. Sharma, R. Prabhakar, V. Srinivasan, V. Ramamurthy, P. Sen, *J. Am. Chem. Soc*. 2021, **143**, 2025.

28) M. Hugenschmidt, D. Jannis, A. A. Kadu, L. Grünewald, S. De Marchi, J. Pérez-Juste, J. Verbeeck, S. Van Aert, S. Bals, *ACS Materials Lett*. 2024, **6**, 165.

29) F. Haase, K. Gottschling, L. Stegbauer, L. S. Germann, R. Gutzler, V. Duppel, V. S. Vyas, K. Kern, R. E. Dinnebier, B. V. Lotsch, *Mater. Chem. Front*. 2017, **1**, 1354.

30) X. Han, J. Zhang, J. Huang, X. Wu, D. Yuan, Y. Liu, Y. Cui, *Nat. Commun*. 2018, **9**, 1294.

31) V. T. Förster, *Ann. Phys*. 1948, **437**, 55.

32) N. J. Hestand, F. C. Spano, *J. Chem. Phys*. 2015, **143**, 244707.

33) J. Sung, P. Kim, B. Fimmel, F. Würthner, D. Kim, *Nat. Commun*. 2015, **6**, 6.

34) F. C. Spano, J. Clark, C. Silva, R. H. Friend, *J. Chem. Phys*. 2009, **130**, 074904.

35) C. F. Holder, R. E. Schaak, *ACS Nano* 2019, **13**, 7359.

36) T. Eder, T. Stangl, M. Gmelch, K. Remmerssen, D. Laux, S. Höger, J. M. Lupton, J. Vogelsang, *Nat. Commun*. 2017, **8**, 1641.

37) J.-L. Bredas, *Mater. Horiz*. 2014, **1**, 17.

38) E. Engel, K. Leo, M. Hoffmann, *Chem. Phys*. 2006, **325**, 170.

39) R. D. Pensack, R. J. Ashmore, A. L. Paoletta, G. D. Scholes, *J. Phys. Chem. C* 2018, **122**, 21004.

40) K. E. Brown, W. A. Salamant, L. E. Shoer, R. M. Young, M. R. Wasielewski, J. *Phys. Chem. Lett*. 2014, **5**, 2588.
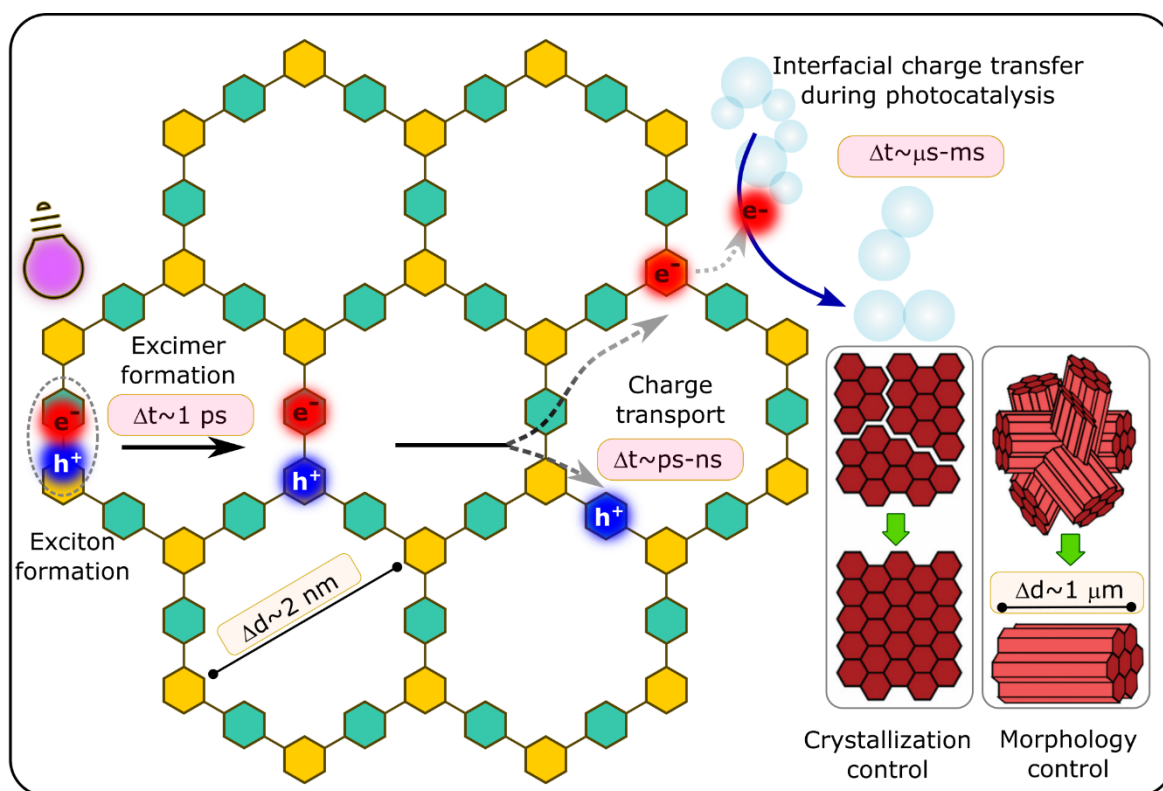
Covalent Organic Frameworks (COFs) are a surging class of extended organic semiconductors routinely used for photocatalysis. However, the charge dynamics intricacies in these materials are still a black box. This work establishes the effect of the physical parameters e.g., morphology and topography of COFs on their photophysical and thereby catalytic properties. Despite having identical chemical structure, the photo-response of COFs can drastically change due the preferential transient intermediates.

[22]